Published in final edited form as:

*J Control Release*. 2019 March 28; 298: 27–37. doi:10.1016/j.jconrel.2019.01.032.

# A nanoliter resolution implantable micropump for murine inner ear drug delivery

**Farzad Forouzandeh**[1], **Xiaoxia Zhu**[2], **Ahmed Alfadhel**[1], **Bo Ding**[3], **Joseph P. Walton**[2,3,5], **Denis Cormier**[4], **Robert D. Frisina**[2,3,5], and **David A. Borkholder**[1,*]

[1]Department of Microsystems Engineering, Rochester Institute of Technology, Rochester, NY, USA

[2]Department of Chemical & Biomedical Engineering, Global Center for Hearing & Speech Research, University of South Florida, Tampa, FL, USA

[3]Department of Communication Sciences & Disorders, Global Center for Hearing & Speech Research, University of South Florida, Tampa, FL, USA

[4]Department of Industrial and Systems Engineering, Rochester Institute of Technology, Rochester, NY, USA

[5]Department of Medical Engineering, Global Center for Hearing & Speech Research, University of South Florida, Tampa, FL, USA

## Abstract

Advances in protective and restorative biotherapies have created new opportunities to use site-directed, programmable drug delivery systems to treat auditory and vestibular disorders. Successful therapy development that leverages the transgenic, knock-in, and knock-out variants of mouse models of human disease requires advanced microsystems specifically designed to function with nanoliter precision and with system volumes suitable for implantation. Here we present results for a novel biocompatible, implantable, scalable, and wirelessly controlled peristaltic micropump. The micropump configuration included commercially available catheter microtubing (250 μm OD, 125 μm ID) that provided a biocompatible leak-free flow path while avoiding complicated microfluidic interconnects. Peristaltic pumping was achieved by sequentially compressing the microtubing via expansion and contraction of a thermal phase-change material located in three chambers integrated adjacent to the microtubing. Direct-write micro-scale printing technology was used to build the mechanical components of the pump around the microtubing directly on the back of a printed circuit board assembly (PCBA). The custom PCBA was fabricated using standard commercial processes providing microprocessor control of actuation and Bluetooth wireless communication through an Android application. The results of *in vitro* characterization indicated that nanoliter resolution control over the desired flow rates of 10–100

*Corresponding author at: Department of Microsystem Engineering, Kate Gleason College of Engineering, Rochester Institute of Technology, 168 Lomb Memorial Drive, Rochester, NY, USA, 14623, **Phone:** +1 585 475 6067, David.Borkholder@rit.edu.

nL/min was obtained by changing the actuation frequency. Applying 10x greater than physiological backpressures and ±3 °C ambient temperature variation did not significantly affect flow rates. Three different micropumps were tested on six mice for *in vivo* implantation of the microcatheter tubing into the round window membrane niche for infusion of a known ototoxic compound (sodium salicylate) at 50 nL/min for 20 minutes. Realtime shifts in distortion product otoacoustic emission thresholds and amplitudes were measured during the infusion. There were systematic increases in distortion product threshold shifts during the 20-minute perfusions; the mean shift was 15 dB for the most basal region. A biocompatibility study was performed to evaluate material suitability for chronic subcutaneous implantation and clinical translational development. The results indicated that the micropump components successfully passed key biocompatibility tests. A micropump prototype was implanted for one month without development of inflammation or infection. Although tested here on the small murine cochlea, this low-cost design and fabrication methodology is scalable for use in larger animals and for clinical applications in children and adults by appropriate scaling of the microtubing diameter and actuator volume.

**Keywords**

Inner ear; Drug delivery; Mouse; Micropump; 3D-printing; Round window membrane; Microfluidics

## 1. Introduction

Hearing loss affects 466 million people worldwide as estimated by the World Health Organization in 2018 [1]. Conventional routes for inner ear drug delivery (i.e., injections and oral delivery) are relatively ineffective, principally because of the blood-cochlear barrier [2–4], delivery to unintended targets, unknown cochlear drug concentration levels, and toxicity [5]. Site-directed, programmable drug delivery systems are needed to leverage recent advances in protective and restorative biotherapies that have created new opportunities to treat auditory and vestibular disorders [6–8].

The cochlea of the inner ear is the specialized organ where auditory perception starts, and is one of the most challenging drug delivery target organs due to its small size and relative inaccessibility. It is surrounded by the temporal bone, which is the hardest bone in the body and the diameters of the coiled tubes within the inner ear are < 2 mm for human. The cellular machinery within the cochlea (e.g., the hair cells in the organ of Corti) are extremely sensitive to mechanical and chemical damage [5]. Successful therapy development for protecting or regenerating cochlear cells which are damaged or missing in cases of hearing loss or deafness, involve the use of transgenic, knock-in, and knock-out variants of human disease in the mouse model system requires advanced microsystems. However, working with mouse models presents new and significant challenges for inner ear drug delivery due to the extremely small size of the mouse cochlea. For instance, the mouse cochlea contains approximately 620 nL of fluid (perilymph)[9] while the human cochlea contains 150-200 μL perilymph [10,11]. This small volume of perilymph in cochlea makes it vulnerable to prolonged or high-flow rate intracochlear delivery [12,13].

To address these challenges for safe and efficacious inner ear delivery, microsystems-based approaches have emerged [14–18]. Such systems require precise and programmable ultra-low flow rates with a controllable profile, due to the small volume of the cochlear perilymph and high sensitivity of the auditory organ to possible damage. Further, a pumping system must be sufficiently small and lightweight, with a planar form factor [19] to be subcutaneously implanted. Also, the system must be robust enough to provide highly controlled, time-sequenced, and ultra-low flow rates over periods of months [5], with the capability of remote activation/deactivation, and programming for automated delivery [8].

These and other considerations limit the applicability of many commercially available inner ear delivery microsystems-based devices. Current osmotic pumps (e.g., Alzet® micropumps) have been used for preclinical experiments for inner ear delivery in larger mammals, including some rodents [20–23]. However, osmotic pumps lack delivery precision and cannot be started or stopped, nor can the flow rate be changed once the infusion is started. Recently, iPrecio® SMP-300 peristaltic micropump was used for infusion of fluorescein isothiocyanate-dextran-labeled dextran as a concentration marker into guinea pig cochlea, using a coupler to connect the tubing of the micropump tubing to a microcatheter [24]. Although these micropumps can provide controlled low flow rates, the overall size and the tubing dimensions are prohibitive for practical subcutaneous implantation in smaller rodents and mice.

Recently inner ear drug delivery microsystems have been an evolving focus of research. A team from Draper Laboratory and the Massachusetts Eye and Ear Institute developed a head-mount reciprocating delivery system for direct intracochlear delivery in guinea pigs utilizing conventional machining and UV laser cutting [8,25]. The system works based on infusion and withdrawal of the drug through the cochlear perilymph. Although it includes a micropump and a drug reservoir, it is too large for implantation, even in the guinea pig. Microelectromechanical system technologies (MEMS) have also been used for fabrication of drug delivery microsystems [26]. In 2016, we reported the development of a miniaturized planar MEMS-based peristaltic micropump for nanoliter cochlear perfusion [27]. However, the device had to overcome significant microfluidic interconnection challenges [28] to allow integration of sub-mm scale in-plane microcatheter tubing without adding significant micropump volume.

In addition to microfluidic interconnect challenges, incorporation of control electronics to MEMS-based micropumps can be accomplished either through expensive application specific integrated circuits integrated on-chip, or via a separate PCBA that adds significant bulk to the assembled system Scaling of MEMS-based systems also requires modification of the fabrication processes and masks, creating challenges for scalability to human clinical translation.

Here we present a novel miniaturized, wirelessly controlled, fully implantable, and scalable peristaltic micropump that provides programmable and accurate drug delivery for inner ear applications. The actuation force of the micropump is provided by expansion/shrinkage of a thermally phase-change material due to its melting/crystallization. The micropump uses 3D-printing technology and is built directly on the backside of a PCBA around microcatheter

tubing (OD=250 μm, ID=125 μm) to integrate the mechanical and control electronic components. The flow path is leak-free and biocompatible and is free of complex microfluidic interconnects. The results of our *in vitro* characterization indicated that the micropump provided nanoliter control of flow rates against ten times greater than physiological backpressures. The *in vivo* mouse model system results indicate functional round window membrane (RWM) drug delivery. Biocompatibility was explored using *in vitro* and *in vivo* experiments.

## 2. Materials and methods

### 2.1 System overview and concept

Using a sub-millimeter microcatheter tubing as the fluid-carrying component limits the options for pumping approaches. Methods that require the use of in-line rectifying valves result in bulk that is unacceptable for size-constrained applications. We used peristalsis with the microcatheter tubing sequentially compressed in three locations to induce directional flow. Peristaltic micropumps that use a single tube are one the most reliable mechanisms for drug delivery because one medium is in direct contact with the working fluid (drug) and no valves or moving components are in the flow channel, which eliminates contamination, leakage, and dead volumes, and reduces clogging and bubble generation. They also benefit from typical advantages of peristaltic micropumps such as resistance to high backpressure [29–31], bubble tolerance, endurance [32], and self-priming and bi-directional flow capability [30].

Different actuation schemes (e.g., piezoelectric [33–35], pneumatic [36], thermopneumatic [37], electrostatic [38], and phase-change [27]) are used for peristaltic micropumps. In this study, a novel phase-change actuation method has been used due to its low driving voltage, significant displacement, small size, and high actuation force enabling effective pumping against backpressure. The actuation material was encapsulated in the body of the micropump surrounded by stiff structures except for one side that is exposed to the deformable microcatheter tubing. Peristalsis occurred as a consequence of sequential melting and solidification and associated expansion and shrinking of the phase-change material which drove cyclic compression and release of the microcatheter tubing. Various phase-change materials can be used for actuating micropumps (e.g., gallium [27] and paraffin wax [39]). Paraffin wax was used as the actuation material, due to its stable phase-change behavior and high-pressure actuation [40]. In addition, the paraffin wax melting point can be chosen for a desired application by selecting the appropriate molecular weight of the wax.

The micropump was built directly on the back of a printed circuit board (PCB) employing 3D-printing technology. Three pairs of resistive heaters and thermistors were placed on the PCB to make a linear template for three chambers and a groove between them for the microcatheter tubing. The three chambers were fabricated in the designated linear pattern adjacent to the microcatheter tubing and were separated by 1.2 mm. Paraffin wax was precisely deposited in the chambers. A peristaltic sequence was applied to the micropump, with a timing control ensuring two closed chambers at each moment. The chambers closed in a sequence of 1 and 3, 1 and 2, and 2 and 3, which pumped the fluid from left to right. Figure 1 shows schematic views of the actuation mechanism and the micropump.

## 2.2 Electronics

The control electronics for actuation and control were fabricated on the front of the four-layer PCB. Off-the-shelf components were used for the micropump control electronics, which were designed for ultra-low-power operation. A rechargeable lithium polymer battery provided power to the system A step-down buck converter (TPS62743, Texas Instruments) was chosen to provide sufficient current output (300 mA maximum) during pumping, a high efficiency (up to 90% at 10 μA load), and low quiescent current (360 nA) when the system is in shutdown mode. Each pump chamber included a thermistor and a 40-ohm resistive heating element with a discrete N-type metal-oxide-semiconductor for controlling temperature. A 1.8-V power rail was used for the entire system to optimize the power consumption of the wireless microcontroller.

The system on a chip (CC2640, Texas Instruments) included an integrated Bluetooth low energy transceiver (BLE 4.2), a 32-bit ARM Cortex-M3 processor with an up to 48 MHz clock speed, and an ultralow-power sensor controller. This system was chosen for its shutdown current of 100 nA since the system will spend the majority of time in deep sleep mode when the pump is not actively delivering drugs. The system's real time clock used a 32-kHz oscillator (SiT1532, SiTime) based on silicon MEMS technology; it had the smallest footprint and lowest power consumption of commercially available oscillators. A wire antenna with a length of 10 mm was chosen to keep the overall device footprint as small as possible. The control electronics were configured and operated using a custom Android application via BLE. Figure 2 shows an image and the block diagram of the fabricated electronics.

## 2.3 Heat transfer analysis

Thermal actuation with phase change materials requires effective transfer of heat in and out of the medium. Heat transfer rates limit actuation frequency and flow rate and affect power consumption. To optimize the micropump system design, a 3D heat transfer model was developed in COMSOL Multiphysics®. In these simulations, the wax remains solid with phase change modeled via changes in heat capacity in the melting temperature range, a common simplification for wax phase change analysis [41,42]. The four copper layers, copper paths, PCB, resistors, thermistors, wax, and resin that covered the entire system were the elements that most affected the system heat transfer properties. The geometric details of these elements were designed using SolidWorks® and imported into COMSOL Multiphysics®.

A user-defined function (UDF) was used to model the phase-change phenomenon based on the apparent heat capacity method. In this UDF, the phase-change energy of the wax was spread over the phase-change temperature range of 4 °C [43,44]. This model analyzed the thermal behavior of the system based on material properties, geometry, the difference between the wax melting point and the ambient temperature, and ambient heat transfer characteristics. This generic model can be used for various ambient temperatures and selected wax molecular weights (ie. melting point) to evaluate and optimize pump performance. To present generalized results, all temperatures were presented relative to the ambient temperature..

The material properties of the different elements were considered using the COMSOL library and material datasheets. To simulate *in situ* application of a subcutaneously implanted system (i.e., in the mouse), the micropump outer surface boundary condition was set at free convection in water. A UDF enabled sequential heating of the resistive heaters in the chambers based on the desired actuation frequency. The wax temperature was fixed at the set temperature using a UDF for the heat generator to apply a closed-loop on-off controller based on the temperature reported by the thermistor. This simulated micropump heat generation and feedback control.

The results of the heat transfer analysis were first validated using a micropump model. To achieve the maximum target flow rate of 100 nL/min high actuation frequencies were required. Therefore, the design and phase-change material optimizations were i) a 10 °C differential between the wax melting point and the ambient temperature, and ii) reduction from 36 μm (1 oz) to 18 μm (0.5 oz) of the thickness of the copper in the PCB. This thickness reduction increased the actuation frequency by 14% due to reduced thermal mass and heat transfer away from the chamber. The addition of a copper pad to the bottom of each chamber improved the homogeneity of the chamber temperature distribution by 33%.

The ability of the system to operate at the required frequencies and the insulation between the chambers were studied using the model with the optimized material and geometry. Figure 3A shows the simulated temperature elevations when applying 0.33 Hz actuation signals, which theoretically can provide the target flow rate of 100 nL/min. Six pumping cycles were simulated, and the results indicated that the chamber temperatures could fluctuate between the wax melting point and 5 °C lower, which allowed the wax to melt and solidify during each cycle without thermal saturation. The results of a steady state simulation with chambers 1 and 3 on and chamber 2 off indicated that the chambers were well-insulated (Figure 3B). While two side chambers were set at the melting point, the middle chamber maintained a temperature approximately 9 °C cooler than the melting point.

A crucial characteristic for implantable devices is that the surface temperature should not exceed 2°C above ambient temperature. The results of the transient simulations were examined to estimate temperature increases in the micropump exterior surface. It was found that the micropump surface temperature was never >0.3 °C higher than the ambient temperature.

### 2.4 Fabrication process

A new fabrication process was developed using 3D-printing technology. The mechanical structure of the micropump was direct-write printed on the back of a 0.7-mm thick standard FR4 PCBA. The control electronics were populated on the front side using standard PCB assembly technology. Three pairs of thermistors and resistors were assembled on the back of the board in a linear offset formation to accommodate subsequent placement of the microcatheter tubing. The micropump structure was 3D-printed using a polymer inkjet printer (Roland VersaUV LEF-12, Tokyo, Japan) and an ECO-UV® resin; three circular chambers with 1.3 mm diameter and 0.35 mm height were printed around the resistor/thermistor pairs, along with a groove for the microcatheter tubing.

Polyurethane-based catheter microtubing (ID=125 μm, OD=250 μm; Micro-Renathane® Catheter Tubing, Braintree Scientific Inc., MA, USA) was placed, fixed, and sealed in the groove using cyanoacrylate resin. A precise volume (240 nL) of nonadecane ($CH_3(CH_2)_{17}CH_3$; Sigma-Aldrich, USA) was deposited in each chamber, ensuring complete coverage of the resistor/thermistor pairs and the microtubing on all surfaces. Cyanoacrylate resin was used to cover and seal the structure and to provide mechanical strength to avoid deformation due to phase-change pressure. Finally, the micropump was encapsulated with an approximately 2-μm-thick layer of parylene-C (Specialty Coating Systems, Indianapolis, Indiana) using a custom-built parylene deposition tool. The parylene-C coating provided a biocompatible moisture barrier around the micropump, enabling electrical insulation for the electronics.

## 2.5 In vitro characterization

The micropump was first characterized using *in vitro* experiments. Flow rate measurements were taken at different actuation frequencies, backpressures, and ambient temperature variations. The actuation temperature of each chamber was calibrated across the range of actuation frequencies and ambient temperatures. The micropump was submerged in deionized (DI) water in a petri dish to simulate the thermal characteristics of the pump after implantation. Nanofittings (Idex©, WA, USA) were used to connect the tubing to a Luer Lock syringe. The micropumps were specifically designed for room temperature operation.

The micropump was powered by a 3.7 V rechargeable Li-ion battery and was programmed by an Android application. Dyed DI water was used as the working fluid to provide visual observation of the fluid displacement in the microcatheter. The fluidic system was filled and visually inspected for no trapped air. The downstream microtubing was placed on a ruler with the flow rate measured by calculating fluid front advancement in the 125 μm ID microcatheter.

## 2.6 In vivo Experiment

An *in vivo* test of the system was performed using a paradigm that induces temporary hearing loss via administration of sodium salicylate following a protocol developed at our laboratory [45]. Salicylate causes reversible disruption of outer hair cell motility because it can act as a competitive antagonist at the anion-binding site of prestin [46]. Disruption of prestin reduces the magnitude of otoacoustic emissions [47] and can result in reduced distortion product (DP) amplitudes and reversible elevation of distortion product otoacoustic emission (DPOAE) thresholds. Thus, salicylate was delivered to the RWM and auditory function was assessed using DPOAE methodology.

### 2.6.1 Drug infusion system and solutions—

The salicylate solution consisted of NaCl (120 mM), KCl (3.5 mM), CaCl2 (1.5 mM), glucose (5.5 mM), HEPES buffer (4-(2-hydroxyethyl)-1-piperazineethanesulfonic acid, 20 mM), and sodium salicylate (50 mM). The pH was adjusted to 7.5 using NaOH. All solutions were prepared on the day of the experiment using sterile double-distilled water. The salicylate was loaded into a 3-cc sterilized syringe and was debubbled. Using positive pressure, the salicylate was pushed until it was 1 mm from the tip of the tubing and then the micropump was placed on the same

level as the mouse. After each experiment, sterile, double-distilled water, was forced through the tee, fittings, and microcatheter tubing in order to clean the fluidic elements.

**2.6.2 Animal and surgical procedures—**A total of six young adult (age, 2–4 months) CBA/CaJ mice bred and raised in-house were used for this study. Each animal underwent a bullaostomy surgery to prepare a site for infusion of the salicylate into the middle ear cavity. All animal procedures were approved by the University of South Florida Institutional Animal Care and Use Committee and were performed using National Institutes of Health and veterinary standards of care.

Each animal was deeply anesthetized for the bullaostomy surgery using a mixture of ketamine (120 mg/kg body weight) and xylazine (10 mg/kg body weight) injected via the intraperitoneal route. The left ventral surface of the neck was then shaved and cleaned. The animal was positioned on its back on a heated operative plane maintaining aseptic conditions. Surgery was performed on the left (ipsilateral) ear following procedures performed by Borkholder *et al.* [45]. Briefly, the tympanic bulla was exposed using a ventral approach, and an incision was made in a longitudinal direction along the ventral surface of the neck to expose the bulla. A 300-μm diameter carbide micro drill bit modified to include insertion stops was used to bore a bullaostomy at a location approximately 1.5 mm laterally below the stapedial artery [14]. Using a micromanipulator (MM3–3, World Precision Instruments, Sarasota, FL), a fine metal probe was attached to the polyimide infusion tubing using adhesive (3M Repositionable 75 spray adhesive, St. Paul, MN). The infusion tubing assembly was inserted into the bullaostomy to a depth of approximately 300–500 μm, near the opening of the round window. Medical grade adhesive (Loctite 4206, Rocky Hill, CT) was used to temporarily secure the infusion tubing to the bulla opening. Subsequent application of dental cement (3M ESPE Duralon) provided a more permanent and robust bond and sealed the cannula to the bullaostomy site. The surgery site was loosely sutured closed to provide strain relief for the infusion tubing. During infusions, each mouse was immobilized using anesthesia as described in this section. Supplementary doses at one-third of the initial dose were administered as needed to maintain the proper levels of general anesthesia. After each infusion, the pump was stopped, and anesthesia was maintained for an additional 40 minutes while additional auditory assessment data were recorded.

**2.6.3 Auditory function assessment—**The auditory function measures were the same as we previously reported [48]. Each mouse was anesthetized as described in section 2.6.2. Supplementary doses of anesthetic were administered as needed. Auditory function was assessed via automated DPOAE threshold measurements at F2 frequencies of 8.9 kHz, 13.5 kHz, 17.9 kHz, 24.6 kHz, 35.8 kHz, and 51.4 kHz. Measurements performed before surgery were used for a baseline to compare subsequent DPOAE threshold shifts.

Stimuli (F1 and F2) were generated using Tucker Davis hardware (TDT; Alachua, FL) controlled via ActiveX from a custom Matlab r13 (Mathworks; Natick, MA) graphical user interface. A Tucker Davis RP2.1 processor at a sample rate of 200 kHz was used to generate the sound stimuli and acquire the signals. All acoustic signals were emitted through electrostatic speakers (TDT EC1) connected to a probe via 4-cm tubes. The probe contained an ER10B+ microphone (Etymotic; Elk Grove Village, IL). Waveforms from each

presentation were windowed using a Hamming window, and high-resolution 390625-point fast Fourier transforms (FFTs) (2× sample rate) were calculated. The resulting FFTs had a bin size of 0.5 Hz, which allowed for accurate measurement of signal level as a function of frequency. Frequency-domain averaging was used to minimize artifacts. Before subsequent analysis, the mean FFT values for multiple repetitions of the same stimulus were calculated. The probe microphone was calibrated relative to a 0.25” B&K microphone (Type 4938, Bruel & Kjaer; Naerum, Denmark) using a 0.1 cc coupler (simulating the mouse ear canal).

DPOAE amplitudes were measured by generating F1 and F2 primaries at 65 and 50 dB sound pressure leve (SPLs), respectively (ratio of the two frequencies = 1.25). The output waveforms of the ER10B+ probe microphone were input to a TDT RP2.1 processor. The FFT values for each presentation were averaged and signal levels at five frequencies were sampled (F1, F2, DP (2F1-F2), as well as two noise bins above and below the DP frequency). After FFT sampling, the dBV was converted to SPL based on the ER10B+ microphone calibration. DPOAE thresholds were defined as the F1 level required to produce a DP of 0 dB SPL (+/−1 dB). We developed an automatic threshold search algorithm implemented in Matlab r13 using TDT hardware and the Etymotic ER10B+ probe microphone.

### 2.7 Biocompatibility

Biocompatibility of all materials in contact with the drug or tissue was assessed before chronic subcutaneous implantation tests. The biocompatibility experiments were performed on key micropump components: the micropump tubing, parylene-coated tubing, and Polydimethylsiloxane (PDMS). PDMS will be used for the subcutaneous implantation tests. An early step in this process involved performing a cell growth curve to set a baseline for normal cellular growth. The key micropump components were then added to assess effects on cell health and viability. Biocompatibility of the material was evaluated by comparing the cell viability assay results when using the micropump materials with the control baseline cell growth viability results (i.e., without use of the pump materials).

The first experiment established the health and viability of the control cells. The growth of random samples of human mammary epithelial cells (ATCC-HMEC cell line) was recorded. Each day for 11 days, ten random samples of human mammary epithelial cells were removed from a 75 $cm^2$ flask. Cell numbers were assessed in a cross-sectional area of 0.5 mm by 0.5 mm, or 700 pixels by 700 pixels, using the cell counter program NIH-ImageJ. Five cross-sectional areas were chosen for each sample (Figure 4). The first area was taken from the top left, the second from the top right, the third from the center, the fourth from the bottom left, and the fifth from the bottom right of the photograph (Figure 4). The cells that were on the boundaries of the top and left sides of the boxes were counted, and the cells that were on the boundaries of the bottom and right sides of the box were not counted. The results were recorded in a Microsoft Excel spreadsheet, the mean values for the five cross-sectional areas for each sample were calculated, and the mean results for each day were estimated. The days and mean cell numbers were graphed to display a cell growth curve that showed the growth of the cells over time.

The second experiment was performed for quantitative assessment of the cell viability of the control cells (no pump parts) versus the cells grown in the presence of key pump components. The cell viability assays used included the XTT, MTT, and BDRU tests of cell health and viability. These *in vitro* assays are a first step towards ISO 10993 biocompatibility tests, which are more involved *in vivo* tests of toxicity, irritation and hemocompatibility. If the *in vitro* assays of the present report show biocompatibility of the pump parts, then the more extensive ISO 10993 tests should be undertaken. The ATCC-HEMC human epidermal epithelial cell line was used for the biocompatibility and viability tests here. The cells were seeded into 96-well culture plates, the groups were set up as non-treated and treated (e.g., parylene, PDMS, pump tubing, or a combination) groups for 2 or 7 days. Each experiment was repeated three times.

For the MTT assay [49], the cells were seeded in 96-well culture plates and exposed to different conditions. Then, 20 μL MTT (5 mg/mL stock solution) was added to each well, and the plates were incubated at 37 °C for 5 hours. Thereafter, the medium was gently removed from each well, and 200 μl DMSO was added to each well to dissolve the purple formazan crystals. The absorbance at 570 nm wavelength was recorded using the Dynatech MR5000 spectrophotometer (Dynatech Laboratories, Inc., Chantilly, VA).

For the XTT assay [50], the electron coupling solution was added to XTT reagent (1:50 volume ratio) to make an XTT detection solution (Cell Signaling, #9095). Five ml XTT solution and 0.1 ml electron coupling solution were added to each well. Then 50 μL XTT detection solution was added to each well that contained the 100–200 μl/well culture medium and the plate was returned to the incubator. Absorbance at a 450-nm wavelength was recorded. The optimal incubation time for this assay depended on the experimental setup (e.g., cell type, cell number, and treatment). Optimization of incubation time was determined by reading one plate at various time points after addition of the XTT detection solution.

The BRDU-test was performed according to the manufacturer's instructions (Cell Signal kit #6813). Cells were seeded in each well of a 96-well plate, then 100 μL/well Fixing/Denaturing Solution was added to each well. The solution was removed after a 30-minute incubation at room temperature. Prepared 1X detection antibody solution (100 μL/well) was then added, and the plate was incubated at room temperature for 1 hr. The solution was discarded, and the plate was washed three times with the 1× Wash Buffer. Prepared 1× HRP-conjugated secondary antibody solution (100 μL/well) was then added and the plate was incubated at room temperature for 30 minutes. The solution was removed, and the plate was washed three times with the 1× Wash Buffer. TMB Substrate (100 μL/well) was then added, the plate was incubated for 30 minutes at room temperature, the STOP Solution (100 μL) was added. Absorbance (450-nm wavelength) was then measured. To obtain the most accurate result, the absorbance was recorded within 30 minutes after adding the STOP Solution.

## 3. Results and discussion

The completed micropump is illustrated in Figure 5A. The overall pump size is 8 × 8 × 3 $mm^3$ (L × W × H). *In vitro* experiments were performed to assess the capacity of the micropump to provide required flow rates for inner ear drug delivery in the presence of physiological backpressure. The consistency of the micropump to provide a 50 nL/min delivery flow rate during a 20-minute period was also examined. This flow rate was required for the *in vivo* experiments. Finally, the micropump performance was tested at different ambient temperature conditions because after subcutaneous implantation the micropump may be exposed to variations in ambient temperature. *In vivo* experiments test three micropumps in six mice with the microcatheter tubing implanted at the RWM niche delivering salicylate at 50 nL/min for 20 minutes, replicating a previous drug delivery system utilizing syringe pump instead of micropumps [45]. Auditory function was assessed using the DPOAE method.

### 3.1 Micropump performance characterization at physiological backpressures

Flow rates were measured at actuation frequencies from 0.015 Hz to 0.21 Hz (i.e., 0.015 Hz, 0.05 Hz, 0.1 Hz, 0.15 Hz, 0.21 Hz) to provide 10-100 nL/min, which covers two times above the maximum reported drug delivery infusion flow rate [17,18,45,51]. The backpressures were 0 and 5 kPa, which covered one order of magnitude larger than the endolymphatic physiological backpressures of 0.33–0.53 kPa in the guinea pig [52] (no measurements were available for the mice). The results (Figure 5B) indicated that the micropump can provide almost linear results ($R^2$= 0.98) through the 10–100 nL/min range, suggesting wax melting / crystallization kinetics are not a limiting factor in micropump performance across the actuation frequencies explored. The results also indicated that applying 5 kPa backpressure did not significantly affect the flow rate.

### 3.2 Pump performance at different ambient temperatures

Pump performance was characterized at different ambient temperatures to evaluate functionality after implantation, considering the possible variation in the body temperature and ambient temperature. The experiments were performed at 0.015 Hz, 0.1 Hz, and 0.21 Hz actuation frequencies, which represented the minimum, middle, and maximum frequencies, respectively. The ambient temperature was changed to $T_{amb}$-3, $T_{amb}$, and $T_{amb}$+3 to assess the functionality of the micropump at a ±3°C variation from the ambient temperature. The results indicated that the ambient temperature had a minor effect on the micropump flow rate (i.e., < 5% change) (Figure 5C).

### 3.3 Long-term performance

The system was tested using a mouse model system inner ear drug delivery paradigm [45] in which salicylate was delivered to the RWM niche for 20 minutes at 50 nL/min using a syringe pump. To test the capacity of the micropump to replicate the same experiment, it was set to provide 50 nL/min for 20 minutes (Figure 5D). The results indicated that the micropump provided an average flow rate of 50.2 nL/min (standard deviation = 0.96 nL/min). The flow rate fluctuation was approximately ±2%, and 1,004 nL drug was delivered over the 20 minute period (0.4% error).

### 3.4 Flow rate resolution

Characterization of micropump resolution at different flow rates included the entire suggested range of 10–100 nL/min. Experiments were performed at 10, 50, and 100 nL/min to test the minimum, *in vivo* infusion, and maximum flow rates, respectively (Figure 5E). For the 10 nL/min rate, the actuation frequencies were changed by 0.00075 Hz until the flow rate was statistically different compared with the reference flow rate of 9.94 nL/min. The lowest resolution for this flow rate was 1.24 nL/min. For the 50 and 100 nL/min rates, the actuation frequencies were changed by 0.0025 Hz until the differences were statistically significant. The lowest resolutions for the 50 and 100 nL/min rates were 2.35 and 2.39 nL/min, respectively. Therefore, the worst-case flow rate resolution was 2.39 nL/min.

### 3.5 In vivo characterization of the micropump

*In vivo* experiments were performed using three mice. A cannula connected to the same micropump was placed near the RWM. Figure 6 shows the effect of RWM perfusion of sodium salicylate delivered at a 50 nL/min flow rate. The effects on the DPOAE threshold shifts were recorded from three different mice over the course of 20-minutes. The results for the mean threshold shifts are presented in panel A and compare the changes in DPOAE thresholds to baseline at four time points (i.e., post-surgery (PS) in which DPOAE values were acquired immediately before the pump was turned on, 0 minutes, the time at which the pump was turned on, and 10 and 20 minutes following the onset of salicylate perfusion. See supplemental Figure 1 for SEMs at each measurement. A baseline measurement was acquired approximately 10–15 minutes before the cannula placement surgery was performed. There was a systematic increase in threshold shift during the 20-minute perfusion; there was a mean shift of 15 dB for the most basal region. In this case, the same pump was used for the three different mice. Panel B presents the results for the period for a mean threshold shift at 51 kHz. The perfusion was stopped at 20 minutes and DPOAE values were continuously recorded.

Figure 7 shows the DP threshold shift for three different pumps implanted in three mice in which sodium salicylate was perfused. The actual threshold shift was referenced to the baseline condition. The time course of the threshold shift or the loss of outer hair cell motility due to dysfunction in prestin was consistent across the three micropumps. The maximum shift was between 15 to 29 dB and was observed in the most basal (51 kHz) cochlear location consistent with salicylate delivery to the RWM niche.

### 3.6 Biocompatibility

The results of the control cell line growth experiment indicated that the numbers of cells increased each day and cell morphology became more developed over time (Figure 8A). The results for the cell growth function for the cell culture used and the predicted theoretical exponential cell growth curve are presented in Figure 8B. The close correspondence between the two functions indicated normal, healthy cell growth and healthy and viable cell cultures. Based on the results of the cell growth curve, during the subsequent experiments cell growth was measured on days 2 through 7 because during this period cell growth approached linearity and was the most substantial.

For the second experiment, key pump components were added separately or combined to the cell culture dishes. Cell viability assays were performed on Days 2 and 7. A representative micrograph of a cell culture dish with the tubing placed within the growing cells is presented in Figure 8C. The quantitative results for the three-cell health and viability assays, compatible with the ISO 10993 standard tests for implantable medical device biocompatibility, for Day 7 are presented in Figure 8D. In each case, the assays were performed with the materials alone as a comparison condition, then with the pump component materials in the cell culture dishes with the growing cells. The control condition (far right bar on the histograms) provided the cell viability measurements for the cells alone (i.e., no pump components in the cell culture dish). The main finding was that there were no statistically significant between-group differences for cell health, biocompatibility and viability for any of the pump component conditions compared with the control condition.

After successful completion of *in vitro* biocompatibility testing of the pump materials, we implanted a subcutaneous prototype pump on the back of a young adult CBA/CaJ mouse (Figure 9). The power supply connector was exposed on the top of the skull. The mouse recovered, and no morbidity was observed following the implantation. Postimplantation, the mouse was monitored daily and the results indicated that the overall health was excellent. There were no statistically significant body weight changes; any signs of inflammatory or immune responses, or any indications of infection, such as swelling, redness, fever or presence of discolored fluid. Future studies will examine the tissue surrounding the implanted pump systematically for histological signs of inflammation *in vivo*.

## 4. Conclusion

We developed a novel miniature, fully implantable, and scalable phase-change peristaltic micropump with wireless control. The micropump was realized using 3D-printing technology to build the mechanical components around catheter microtubing on the back of a PCBA. On the front side of the PCB, the electronic components were assembled to actuate and control the micropump, along with enabling wireless control. *In vitro* characterization results indicated the pump achieved nanoliter-level resolution of delivery in the specified range of 10–100 nL/min in the presence of up to 10x larger than physiological backpressures. Small variations in ambient temperature were found to not significantly affect the results.

An *in vivo* experiment was performed by implantation of the catheter microtubing of three different micropumps in the RWM of six mice for delivery of sodium salicylate. The results indicated that the DPOAE response was consistent across different micropumps and different animals. Implantability of the micropump was assessed using a biocompatibility evaluation of the micropump components and a system prototype. Our findings showed that the micropump components passed key biocompatibility tests, which indicated that they were suitable for translational applications, including subcutaneous implantation in humans and animal models.

This proof of concept *in vivo* success of our advanced micropump technology used in the mouse (cochlea volume ~ 620 nL) indicates translational opportunities. Using appropriate

scaling of the microtubing size and actuator volume, the pump is inherently scalable for use in larger species and clinical applications in children and adults. Our results indicated that this advanced micropump can provide organ-targeted drug delivery to avoid systemic side effects and maximal control of drug concentration and timing parameters. Future work will demonstrate long-term subcutaneous implantation in mice with periodic drug delivery.

## Supplementary Material

Refer to Web version on PubMed Central for supplementary material.

## Acknowledgments

This work was supported by the National Institute on Deafness and Other Communication Disorders of the National Institutes of Health [grant number R01 DC014568].

## 6. References

[1]. Deafness and hearing loss, (n.d.). http://www.who.int/mediacentre/factsheets/fs300/en/.

[2]. Juhn SK, Jung M-K, Hoffman MD, Drew BR, Preciado DA, Sausen NJ, Jung TTK, Kim BH, Park S-Y, Lin J, Ondrey FG, Mains DR, Huang T, The role of inflammatory mediators in the pathogenesis of otitis media and sequelae., Clin. Exp. Otorhinolaryngol. 1 (2008) 117–38. doi: 10.3342/ceo.2008.1.3.117. [PubMed: 19434244]

[3]. Juhn SK, Hunter BA, Odland RM, Blood-labyrinth barrier and fluid dynamics of the inner ear, in: Int. Tinnitus J, 2001: pp. 72–83. http://europepmc.org/abstract/med/14689642. [PubMed: 14689642]

[4]. Haynes DS, O'Malley M, Cohen S, Watford K, Labadie RF, Intratympanic dexamethasone for sudden sensorineural hearing loss after failure of systemic therapy, Laryngoscope. 117 (2007) 3–15. doi:10.1097/01.mlg.0000245058.11866.15. [PubMed: 17202923]

[5]. Pararas EEL, Borkholder DA, Borenstein JT, Microsystems technologies for drug delivery to the inner ear, Adv. Drug Deliv. Rev. 64 (2012) 1650–1660. doi:10.1016/j.addr.2012.02.004. [PubMed: 22386561]

[6]. Kang WS, Sun S, Nguyen K, Kashemirov B, McKenna CE, Hacking SA, Quesnel AM, Sewell WF, McKenna MJ, Jung DH, Non-Ototoxic Local Delivery of Bisphosphonate to the Mammalian Cochlea., Otol. Neurotol. 36 (2015) 953–60. doi:10.1097/MAO.0000000000000786. [PubMed: 25996080]

[7]. Mizutari K, Fujioka M, Hosoya M, Bramhall N, Okano HJ, Okano H, Edge ASB, Notch Inhibition Induces Cochlear Hair Cell Regeneration and Recovery of Hearing after Acoustic Trauma, Neuron. 77 (2013) 58–69. doi:10.1016/j.neuron.2012.10.032. [PubMed: 23312516]

[8]. Tandon V, Kang WS, Robbins TA, Spencer AJ, Kim ES, McKenna MJ, Kujawa SG, Fiering J, Pararas EEL, Mescher MJ, Sewell WF, Borenstein JT, Microfabricated reciprocating micropump for intracochlear drug delivery with integrated drug/fluid storage and electronically controlled dosing, Lab Chip. 16 (2016) 829–846. doi:10.1039/C5LC01396H. [PubMed: 26778829]

[9]. Thorne M, Salt AN, DeMott JE, Henson MM, Henson OW, Gewalt SL, Cochlear Fluid Space Dimensions for Six Species Derived From Reconstructions of Three-Dimensional Magnetic Resonance Images, Laryngoscope. 109 (1999) 1661–1668. doi: 10.1097/00005537-199910000-00021. [PubMed: 10522939]

[10]. Buckingham RA, Valvassori GE, Inner ear fluid volumes and the resolving power of magnetic resonance imaging: Can it differentiate endolymphatic structures?, Ann. Otol. Rhinol. Laryngol 110 (2001) 113–117. doi:10.1177/000348940111000204. [PubMed: 11219516]

[11]. Igarashi M, Ohashi K, Ishii M, Morphometric Comparison of Endolymphatic and Perilymphatic Spaces in Human Temporal Bones, Acta Otolaryngol. 101 (1986) 161–164. doi: 10.3109/00016488609132823. [PubMed: 3518332]

[12]. Fridberger A, van Maarseveen JT, Scarfone E, Ulfendahl M, Flock B, Flock A, Pressure -induced basilar membrane position shifts and the stimulus-evoked potentials in the low-frequency region of the guinea pig cochlea., Acta Physiol. Scand. 161 (1997) 239–252. doi:10.1046/j.1365-201X.1997.00214.x. [PubMed: 9366967]

[13]. Pararas EEL, Chen Z, Fiering J, Mescher MJ, Kim ES, McKenna MJ, Kujawa SG, Borenstein JT, Sewell WF, Kinetics of reciprocating drug delivery to the inner ear, J. Control. Release 152 (2011) 270–277. doi:10.1016/j.jconrel.2011.02.021. [PubMed: 21385596]

[14]. Chen Z, Kujawa SG, McKenna MJ, Fiering JO, Mescher MJ, Borenstein JT, Leary Swan EE, Sewell WF, Inner ear drug delivery via a reciprocating perfusion system in the guinea pig, J. Control. Release 110 (2005) 1–19. doi:10.1016/j.jconrel.2005.09.003. [PubMed: 16274830]

[15]. Fiering J, Mescher MJ, Leary Swan EE, Holmboe ME, Murphy BA, Chen Z, Peppi M, Sewell WF, McKenna MJ, Kujawa SG, Borenstein JT, Local drug delivery with a self-contained, programmable, microfluidic system, Biomed. Microdevices. 11 (2009) 571–578. doi:10.1007/s10544-008-9265-5. [PubMed: 19089621]

[16]. Mescher MJ, Swan EEL, Fiering J, Holmboe M, Sewell WF, Kujawa SG, McKenna MJ, Borenstein JT, Fabrication methods and performance of low-permeability microfluidic components for a miniaturized wearable drug delivery system, J. Microelectromechanical Syst. 18 (2009) 501–510. doi:10.1109/JMEMS.2009.2015484.

[17]. Borkholder DA, State-of-the-art mechanisms of intracochlear drug delivery, Curr. Opin. Otolaryngol. Head Neck Surg 16 (2008) 472–477. doi:10.1097/MOO.0b013e32830e20db. [PubMed: 18797291]

[18]. Borkholder DA, Zhu X, Hyatt BT, Archilla AS, Livingston WJ, Frisina RD, Murine intracochlear drug delivery: Reducing concentration gradients within the cochlea, Hear. Res. 268 (2010) 2–11. doi:10.1016/j.heares.2010.04.014. [PubMed: 20451593]

[19]. Cima MJ, Microsystem Technologies for Medical Applications, Annu. Rev. Chem. Biomol. Eng. 2 (2011) 355–378. doi:10.1146/annurev-chembioeng-061010-114120. [PubMed: 22432623]

[20]. Swan EEL, Mescher MJ, Sewell WF, Tao SL, Borenstein JT, Inner ear drug delivery for auditory applications, Adv. Drug Deliv. Rev 60 (2008) 1583–1599. doi:10.1016/j.addr.2008.08.001. [PubMed: 18848590]

[21]. Orita H, Shimogori H, Yamashita H, Unilateral intra-perilymphatic infusion of substance P enhances ipsilateral vestibulo-ocular reflex gains in the sinusoidal rotation test, Neurosci. Lett. 449 (2009) 207–210. doi:10.1016/j.neulet.2008.11.020. [PubMed: 19022352]

[22]. Shimogori H, Yamashita H, Efficacy of intracochlear administration of betamethasone on peripheral vestibular disorder in the guinea pig, Neurosci. Lett. 294 (2000) 21–24. doi:10.1016/S0304-3940(00)01534-2. [PubMed: 11044577]

[23]. Eshraghi AA, Adil E, He J, Graves R, Balkany TJ, Van De Water TR, Local dexamethasone therapy conserves hearing in an animal model of electrode insertion trauma-induced hearing loss, Otol. Neurotol. 28 (2007) 842–849. doi:10.1097/MAO.0b013e31805778fc. [PubMed: 17471110]

[24]. Salt A, Hartsock J, Gill R, Smyth D, Kirk J, Verhoeven K, Perilymph pharmacokinetics of marker applied through a cochlear implant in guinea pigs, PLoS One. 12 (2017) e0183374. doi:10.1371/journal.pone.0183374. [PubMed: 28817653]

[25]. Tandon V, Kang WS, Spencer AJ, Kim ES, Pararas EEL, McKenna MJ, Kujawa SG, Mescher MJ, Fiering J, Sewell WF, Borenstein JT, Microfabricated infuse-withdraw micropump component for an integrated inner-ear drug-delivery platform, Biomed. Microdevices. 17 (2015). doi:10.1007/s10544-014-9923-8.

[26]. Nisar A, Afzulpurkar N, Mahaisavariya B, Tuantranont A, MEMS-based micropumps in drug delivery and biomedical applications, Sensors Actuators, B Chem. 130 (2008) 917–942. doi:10.1016/j.snb.2007.10.064.

[27]. Johnson DG, Borkholder DA, Towards an implantable, low flow micropump that uses no power in the blocked-flow state, Micromachines. 7 (2016). doi:10.3390/mi7060099.

[28]. Johnson DG, Frisina RD, Borkholder DA, In-Plane Biocompatible Microfluidic Interconnects for Implantable Microsystems, IEEE Trans. Biomed. Eng. 58 (2011) 943–948. doi:10.1109/TBME.2010.2098031. [PubMed: 21147591]

[29]. Geipel a, Doll a, Jantscheff P, Esser N, Massing U, Woias P, Goldschmidtboeing F, A novel two-stage backpressure-independent micropump: modeling and characterization, J. Micromechanics Microengineering. 17 (2007) 949–959. doi:10.1088/0960-1317/17/5/015.

[30]. Jang LS, Li YJ, Lin SJ, Hsu YC, Yao WS, Tsai MC, Hou CC, A stand-alone peristaltic micropump based on piezoelectric actuation, Biomed. Microdevices. 9 (2007) 185–194. doi:10.1007/s10544-006-9020-8. [PubMed: 17160705]

[31]. Lin Q, Yang B, Xie J, Tai Y-C, Dynamic simulation of a peristaltic micropump considering coupled fluid flow and structural motion, J. Micromechanics Microengineering. 17 (2006) 220–228. doi:10.1088/0960-1317/17/2/006.

[32]. Berg JM, Anderson R, Anaya M, Lahlouh B, Holtz M, Dallas T, A two-stage discrete peristaltic micropump, Sensors Actuators, A Phys. 104 (2003) 6–10. doi:10.1016/S0924-4247(02)00434-X.

[33]. Cazorla PH, Fuchs O, Cochet M, Maubert S, Le Rhun G, Fouillet Y, Defay E, A low voltage silicon micro-pump based on piezoelectric thin films, Sensors Actuators, A Phys. 250 (2016) 35–39. doi:10.1016/j.sna.2016.09.012.

[34]. Pečar B, Križaj D, Vrtačnik D, Resnik D, Dolžan T, Možek M, Piezoelectric peristaltic micropump with a single actuator, J. Micromechanics Microengineering. 24 (2014) 105010. doi:10.1088/0960-1317/24/10/105010.

[35]. Tanaka Y, A peristaltic pump integrated on a 100% glass microchip using computer controlled piezoelectric actuators, Micromachines. 5 (2014) 289–299. doi:10.3390/mi5020289.

[36]. So H, Pisano AP, Seo YH, Caterpillar locomotion-inspired valveless pneumatic micropump using a single teardrop-shaped elastomeric membrane, Lab Chip. 14 (2014) 2240–2248. doi:10.1039/C3LC51298C. [PubMed: 24812661]

[37]. Chia BT, Liao H-H, Yang Y-J, A NOVEL THERMO-PNEUMATIC PERISTALTIC MICROPUMP WITH LOW TEMPERATURE ELEVATION Department of Mechanical Engineering, National Taiwan University, Taipei, TAIWAN, TRANSDUCERS 2009 - 2009 Int. Solid-State Sensors, Actuators Microsystems Conf (2009) 8–11. doi:10.1109/SENSOR.2009.5285892.

[38]. Kim B, Lee KS, Shannon MA, An electrostatically driven peristaltic micropump with an indium tin oxide electrode, 8th Annu. IEEE Int. Conf. Nano/Micro Eng. Mol. Syst IEEE NEMS 2013 1 (2013) 927–930. doi:10.1109/NEMS.2013.6559875.

[39]. Bodén R, Lehto M, Simu U, Thomell G, Hjort K, Schweitz JÅ, A polymeric paraffin actuated high-pressure micropump, Sensors Actuators, A Phys. 127 (2006) 88–93. doi:10.1016/j.sna.2005.11.068.

[40]. Ogden S, Klintberg L, Thomell G, Hjort K, Boden R, Review on miniaturized paraffin phase change actuators, valves, and pumps, Microfluid. Nanofluidics. 17 (2014) 53–71. doi:10.1007/s10404-013-1289-3.

[41]. Kong Q, Ma J, Che C, Theoretical and experimental study of volumetric change rate during phase change process, Int. J. Energy Res 33 (2009) 513–525. doi:10.1002/er.1498.

[42]. Bodén R, Hjort K, Schweitz J-Å, Simu U, A metallic micropump for high-pressure microfluidics, J. Micromechanics Microengineering. 18 (2008) 115009. doi:10.1088/0960-1317/18/11/115009.

[43]. Li H, Liu X, Fang G, Preparation and characteristics of n-nonadecane/cement composites as thermal energy storage materials in buildings, Energy Build. 42 (2010) 1661–1665. doi:10.1016/j.enbuild.2010.04.009.

[44]. Vélez C, Ortiz De Zárate JM, Khayet M, Thermal properties of n-pentadecane, n-heptadecane and n-nonadecane in the solid/liquid phase change region, Int. J. Therm. Sci. 94 (2015) 139–146. doi:10.1016/j.ijthermalsci.2015.03.001.

[45]. Borkholder DA, Zhu X, Frisina RD, Round window membrane intracochlear drug delivery enhanced by induced advection, J. Control. Release. 174 (2014) 171–176. doi:10.1016/j.jconrel.2013.11.021. [PubMed: 24291333]

[46]. Oliver D, He DZZ, Klöcker N, Ludwig J, Schulte U, Waldegger S, Ruppersberg JP, Dallos P, Fakler B, Intracellular anions as the voltage sensor of prestin, the outer hair cell motor protein, Science (80-.). 292 (2001) 2340–2343. doi:10.1126/science.1060939.

[47]. Brownell WE, Outer hair cell electromotility and otoacoustic emissions., Ear Hear. 11 (1990) 82–92. doi:10.1016/j.bbi.2008.05.010. [PubMed: 2187727]

[48]. Frisina RD, Ding B, Zhu X, Walton JP, Age-related hearing loss: Prevention of threshold declines, cell loss and apoptosis in spiral ganglion neurons, Aging (Albany. NY). 8 (2016) 2081–2099. doi:10.18632/aging.101045. [PubMed: 27667674]

[49]. Raju J, Patlolla JMR, V Swamy M, Raju J, Patlolla JMR, V Swamy M, V Rao C, Diosgenin, a Steroid Saponin of Trigonella foenum graecum (Fenugreek), Inhibits Azoxymethane-Induced Aberrant Crypt Foci Formation in F344 Rats and Induces Apoptosis in HT-29 Human Colon Cancer Cells Diosgenin, a Steroid Saponin of Trigonella foenum g, Cancer Epidemiol. Biomarkers Prev 13 (2004) 1392–1399. http://cebp.aacrjournals.org/content/13/8/1392.short. [PubMed: 15298963]

[50]. Francoeur A-M, Assalian A, MICROCAT: A Novel Cell Proliferation and Cytotoxicity Assay Based on WST-1, Biochemica. 3 (1996) 19–25. http://www.roche-applied-science.com/PROD_INF/BIOCHEMI/No.3_96/pp19-25.pdf.

[51]. Chen Z, Mikulec AA, McKenna MJ, Sewell WF, Kujawa SG, A method for intracochlear drug delivery in the mouse, J. Neurosci. Methods. 150 (2006) 67–73. doi:10.1016/j.jneumeth.2005.05.017. [PubMed: 16043228]

[52]. Inamoto R, Miyashita T, Akiyama K, Mori T, Mori N, Endolymphatic sac is involved in the regulation of hydrostatic pressure of cochlear endolymph, Am. J. Physiol. Integr. Comp. Physiol. 297 (2009) R1610–R1614. doi:10.1152/ajpregu.00073.2009.

## Highlights

- The first implantable micropump designed for mouse inner ear drug delivery
- Peristaltic micropump is scalable, programmable, and wirelessly controlled *in vivo*
- Nanoliter resolution over 10–100 nL/min flow rates at 10x physiological backpressure
- Subcutaneous implantation of a prototype micropump in a mouse for over one month
- Micropump cochlear drug delivery results match our published work using syringe pumps

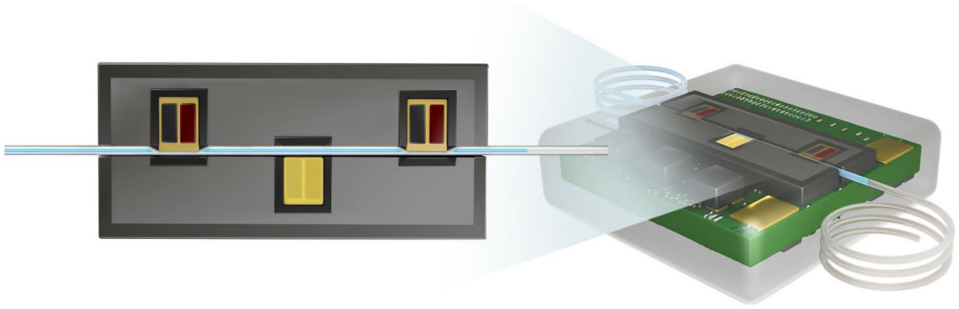

**Figure 1.**

Left) Cyclic phase-change actuation of the three chambers compressed the microcatheter tubing and drove peristalsis. The left and right actuators are in the liquid state, compressing the tubing to eject fluid. Right) Schematic of the peristaltic micropump.

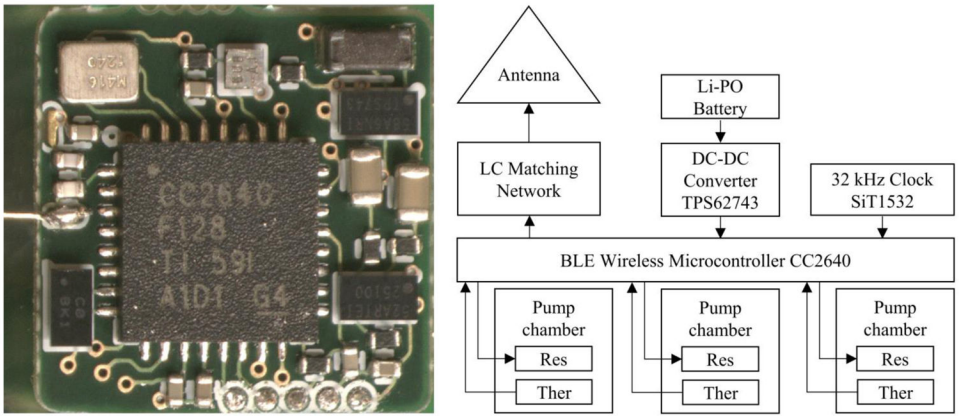


**Figure 2.**

Left) Image of the fabricated electronics on the front side of the printed circuit board. The electronics assembly was used for actuation, closed-loop feedback to control chamber temperatures, and wireless control. Right) Block diagram of the pump control electronics. Res, resistive heater; Ther, thermistor.

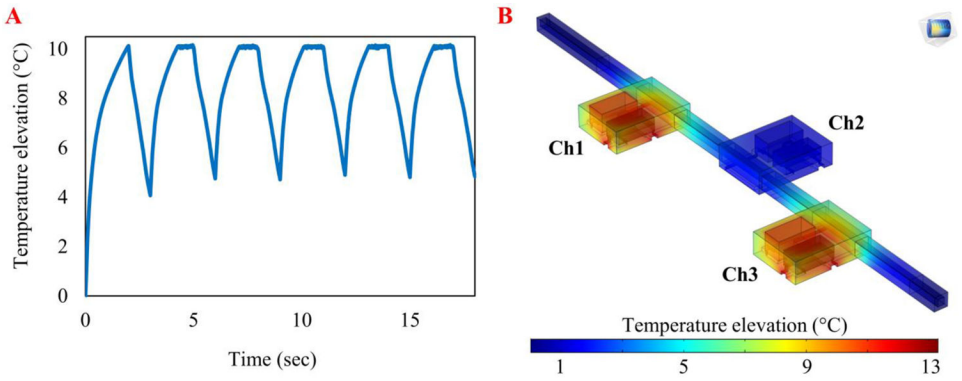


**Figure 3.**

Heat transfer computational analysis of the optimized micropump design demonstrated temperature prediction and control. A) The temperature elevation of chamber 1 during the 0.33 Hz actuation, which is sufficient to provide target flow rate of 100 nL/min. The chamber temperatures cycle between the wax melting point (10 °C higher than the ambient temperature) and 5 °C below the wax melting point, which allowed the wax to melt and crystalize during each cycle. This simulation shows the micropump can work at this frequency without thermal saturation. B) The design provided effective thermal isolation between the chambers. During a steady-state simulation, the average temperatures of chambers 1 and 3 were set at the wax melting point while chamber 2 remained approximately 9°C cooler than chambers 1 and 3. This ensures actuation independence between chambers.

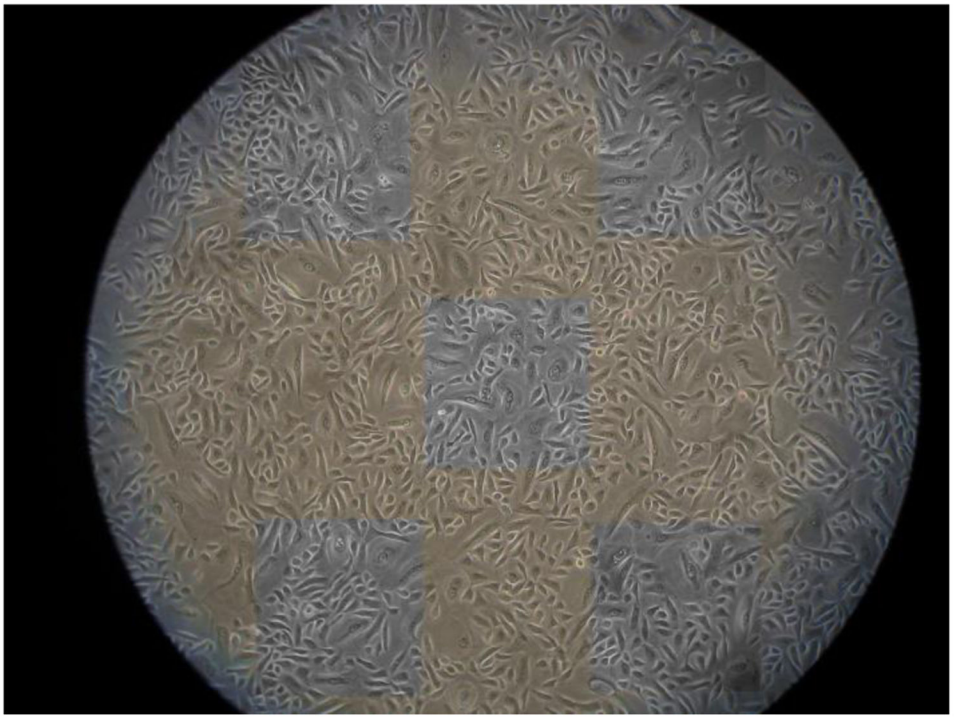

**Figure 4.**

One representative sample from the last day of an 11-day cell growth period. The five areas indicating where cells were counted are illustrated. The mean values from five areas were calculated, and then the total cell counts among the ten samples from Day 11 were averaged to obtain one cell count value for Day 11. Similar analyses were performed on Days 1–10. The data were plotted to obtain the cell growth curves.

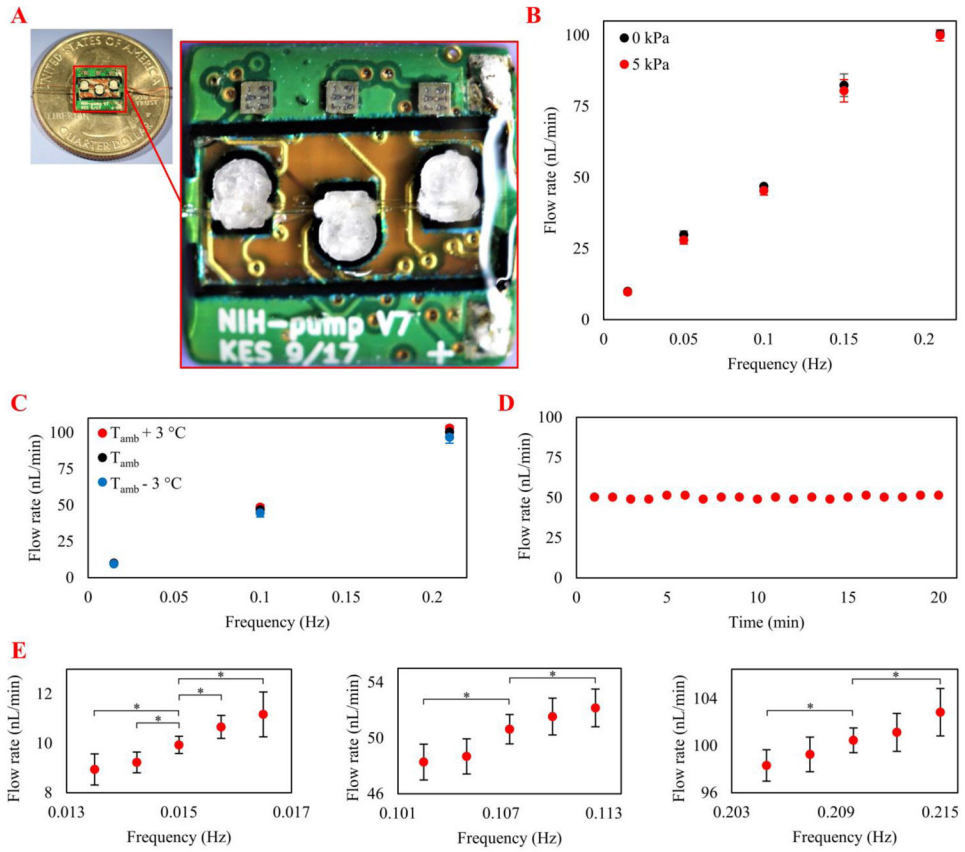


**Figure 5.**

A) Photograph of the peristaltic micropump 3D-printed around a commercially available catheter microtubing on the back of a printed circuit board B) The pump was characterized at 10–100 nL/min flow rates and 0 - 5 kPa backpressures optimized for the intracochlear drug delivery application. Each data point is the mean value of five trials; error bars represent one standard deviation. C) Pump performance at different frequencies and ambient temperatures. The variation in flow rate was not statistically significant by changing the ambient temperature by ±3 °C. Each point is the mean value of five one-minute trials; error bars represent one standard deviation. D) Performance of the pump at 50 nL/min (required for the *in vivo* test) for 20 minutes indicated precise flow rate control. E) Characterization of micropump resolution at flow rates of 10, 50, and 100 nL/min; the greatest resolution was 2.39 nL/min. Each point is the mean value of five trials; error bars represent one standard deviation. Asterisks indicate statistical significance in flow rates by changing actuation frequencies (*$p < 0.05$).

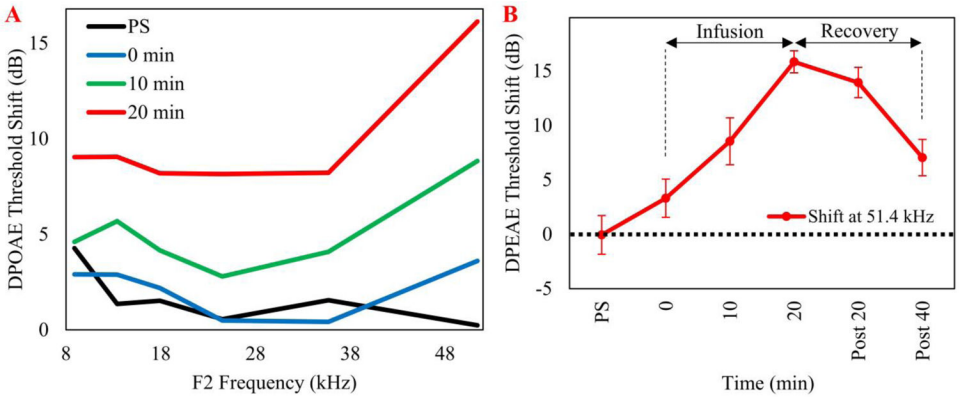


**Figure 6.**

*In vivo* intracochlear delivery of sodium salicylate elevated otoacoustic emission thresholds from 8 to 51 kHz in three mice. In each mouse, the cannula was implanted near the round window via a bullaostomy. A) Mean DPOAE threshold shifts from three mice recorded during 20 minutes after the start of a salicylate infusion. DPOAE thresholds systematically increased as a function of perfusion time from the start of the perfusion (0 minutes) to 20 minutes. B) The mean DPOAE threshold shift for the most basal cochlear region, 51 kHz plotted as a function of time following the start of the sodium salicylate infusion. Post 20 and post 40 min denote the measurement times after turning off the pump. PS = post surgery; post 20 = 20 min after stopping infusion; post 40 = 40 min after stopping infusion. SEMs were less than 3 dB for the conditions tested.

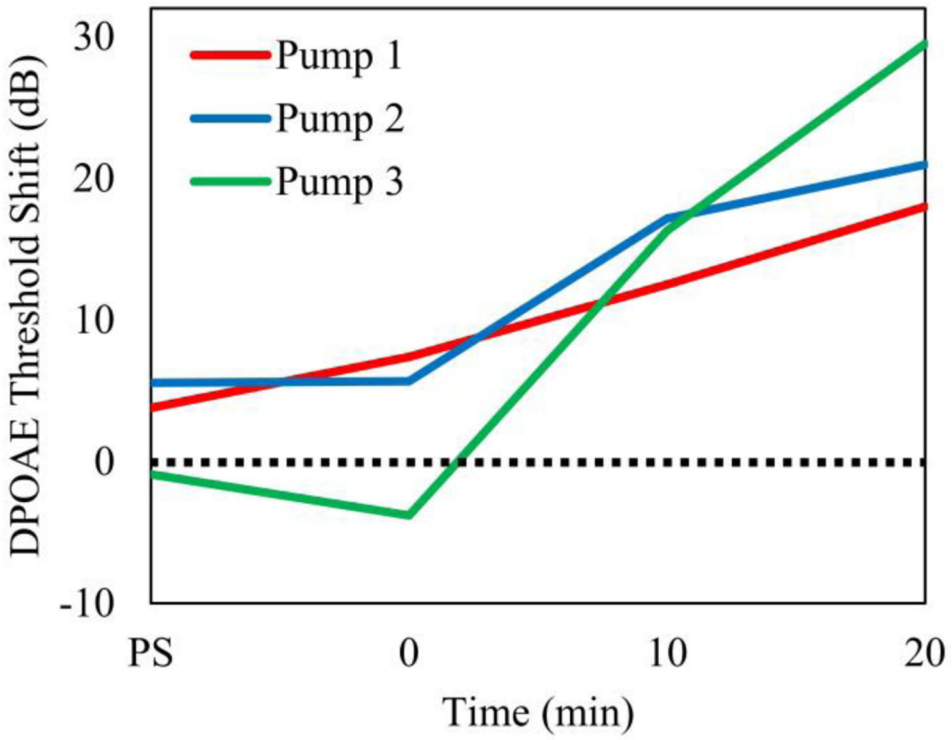


**Figure 7.**
DPOAE threshold shift (51 kHz) for the most basal cochlear region, following sodium salicylate infusion, plotted as a function of time for three micropumps. The time points refer to DPOAE acquired at PS-post surgery, 0 minutes – start of pumping, and 10 and 20 minutes following the onset of pumping.

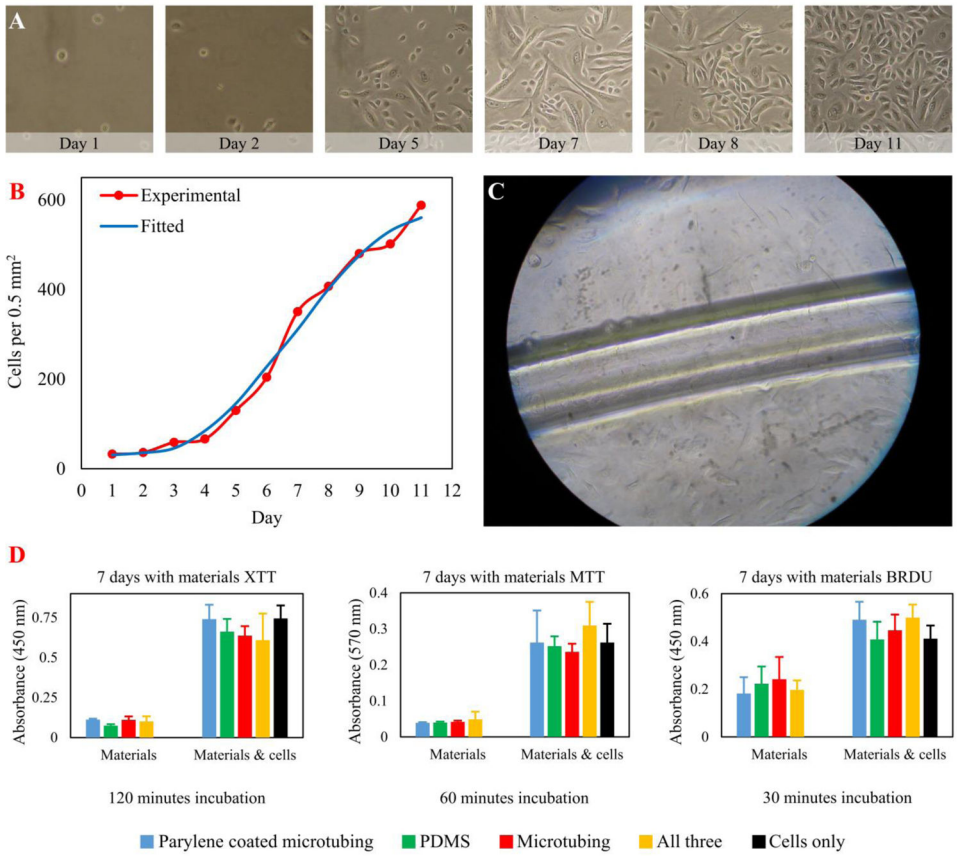


**Figure 8.**

A) Micrographs taken from the center of a sample (Section 3 in Figure 4) at Day 1, Day 2, Day 5, Day 7, Day 8, and Day 11. The photographs illustrate how the numbers of cells increased each day, and that cell morphology became more developed over time. B) Cell growth curve of the human mammary epithelial cells. The curve was similar to the expected exponential growth curve. This result indicated that the cell line used for the cell viability biocompatibility assays met the healthy growth metrics requirement. The curve followed the trend line (blue line, $y= 23.322e^{0.3262x}$) exponential curve, residual value = 0.95. C) Micrograph illustrates the polyurethane-based catheter tubing placed in the well containing human mammary epithelial cells. Under experimental biocompatibility conditions, cells were harvested from the regions directly around the tubing and cell viability assays were performed. The results were quantitatively compared to the cells in the control dishes, which were presented in Figures 4, 8A, and 8B. D) Histogram results indicate there is no statistically significant difference in the cell health and viability quantitative measurements for the human mammary epithelial cells, with and without the pump components. The “materials” measurements represent a comparison condition where only the components were in the dish, with no cells. Under the “materials & cells” conditions, the components were placed in the cell culture dishes on Day 0; the components were in the dishes as the cell size and number increased over a period of 7 days. The far-right bar on the three histograms is the “Cells only” Control condition (i.e., no pump components were present in the dish during cell growth).

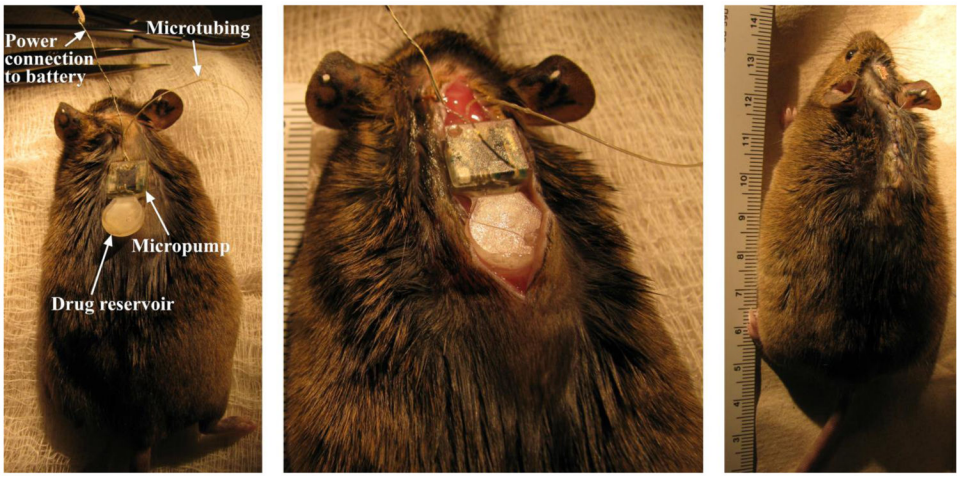


**Figure 9.**

Photos showing the system following subcutaneous implantation in a CBA mouse following one month of implantation. Note the lack of inflammation or infection in the skin surrounding the implant area, and the mouse health and behavior was normal.